A Near-Surface Microstructure Sensor System Used during TOGA COARE. Part I: Bow Measurements

ALEXANDER SOLOVIEV,* ROGER LUKAS, SHARON DECARLO, AND JEFREY SNYDER

School of Ocean and Earth Science and Technology, University of Hawaii at Manoa, Honolulu, Hawaii

ANATOLI ARJANNIKOV AND VYACHESLAV TURENKO

Granit, St. Petersburg, Russia

MARK BAKER

Applied Physics Laboratory, The Johns Hopkins University, Baltimore, Maryland

DMITRY KHLEBNIKOV

P. P. Shirshov Institute of Oceanology, Russian Academy of Sciences, Moscow, Russia

(Manuscript received 13 November 1996, in final form 13 May 1997)

ABSTRACT

High-resolution probes mounted on the bow of the vessel at a 1.7-m depth in an undisturbed region ahead of the moving vessel were used for microstructure and turbulence measurements in the near-surface layer of the ocean during TOGA COARE. The probes measured temperature, conductivity, pressure, three-component fluctuation velocity, and two components of acceleration. Accumulation of large amounts of high-quality near-surface data poses a difficult challenge, and deployment from the bow of a ship, such as is done with these sensors, requires rugged, well-calibrated, and low-noise sensors. The heaving motion of the ship that causes the sensors to break through the surface requires data processing algorithms unique to this application. Due to the presence of surface waves and the associated pitching of the vessel, the bow probes ''scanned'' the near-surface layer of the ocean. Combining the bow sensor's signals with the ship's thermosalinograph pumping water from 3-m depth resulted in the near-surface dataset with both fine temporal/spatial resolution and high absolute accuracy. Contour plots calculated using the bow signals reveal the spatial structure of the diurnal thermocline and rain-formed halocline. The localization in narrow frequency bands of the vibrations of the bow sensors allows calculation of dissipation rates. The characteristics of the sensors and the data processing algorithms related to the periodic surface penetration by the sensors are discussed in this paper.

1. Introduction

A better understanding of microstructure and turbulence in the near-surface layer of the ocean is important to provide boundary conditions for general circulation models; to estimate air–sea fluxes of heat, momentum, and gases; to interpret and calibrate satellite images; and to study the biogeochemistry of the ocean. A region of the ocean where the near-surface processes are of particular importance is the western equatorial Pacific warm pool (Lukas and Lindstrom 1991). This is the domain of the Tropical Ocean Global Atmosphere (TOGA) Coupled Ocean–Atmosphere Response Experiment (COARE). The TOGA COARE project is designed to describe, model, and predict the variability of the coupled ocean–atmosphere system on timescales of months to years (Webster and Lukas 1992). The coupled ocean–atmosphere system in the western Pacific warm pool is very sensitive even to small boundary condition changes. Wind speeds are often small in the western Pacific warm pool. Under low wind speed conditions, substantial temperature, salinity, and current velocity differences can be localized in the upper meters of the ocean (Bruce and Firing 1974; Soloviev and Vershinsky 1982; Kudryavtsev and Soloviev 1990).

Small-scale measurements near the air–sea interface are complicated by the presence of strong sources of perturbations. The orbital velocity of surface waves is

*Current affiliation: Oceanographic Center, Nova Southeastern University, Dania, Florida.

Corresponding author address: Dr. Alexander V. Soloviev, Oceanographic Center, Nova Southeastern University, 8000 North Ocean Drive, Dania, FL 33004.
E-mail: soloviev@ocean.nova.edu

a dominant disturbance. A typical scale of surface-wave vertical orbital velocities is approximately 1 m s^{-1}. Concurrently, the scale of small-scale turbulent fluctuations in the near-surface layer of the ocean is approximately 1 cm s^{-1}. Thus, there is a problem with measuring signals at the air–sea interface because the background disturbance is approximately 100 times stronger than the desired signal.

There are two principal questions associated with collecting small-scale data near the surface. 1) What reference system should be used? 2) How can surface wave disturbances be eliminated from the signal?

A reasonable approach is to make (or at least to interpret) the measurements near the air–sea interface in a Lagrangian coordinate system. Csanady (1984) suggested that ''. . . depth should be expressed in the coordinate system connected with the surface produced by the nearly irrotational component of the wave field.''

Buoy devices (Jones and Kenney 1977; Price et al. 1986; Kudryavtsev and Soloviev 1990; Farmer and Gemmrich 1995), upward rising profilers (Vershinsky and Soloviev 1977; Dillon et al. 1981; Soloviev and Vershinsky 1982; Imberger 1985; Soloviev et al. 1988; Mammen and von Bosse 1990), dropsondes (Bruce and Firing 1974; Azizjan et al. 1984), towed devices (Fedorov and Ginzburg 1992; Thorpe 1985), and bow- or submarine-mounted devices (Stewart and Grant 1962; Volkov et al. 1989; Soloviev 1990; Osborn et al. 1992) have been utilized to obtain measurements in the upper few meters of the ocean. Among the key factors that can affect the quality and interpretation of measurements in the near-surface layer are surface wave perturbations, influence of the ship wake, instability of the sensor motion, impact of bubbles on conductivity (and hence salinity and density) measurements, and strong electrical currents coupled to the water near the vessel due to the ship's electrical field. The sharp vertical gradients in the near-surface physics can also be a factor depending on the measurement approach.

Each approach offers different insights into the near-surface physics and suffers from different limitations. For example, moored buoy measurements are the only approach that yields temporal measurements. However, there is no clear separation in frequency space of the velocity field induced by surface waves or by turbulence. The lack of a dependable mean speed prevents conversion to the spatial domain, which complicates correct estimation of the kinetic energy dissipation rate. Vertical profiling methods can provide such estimates if the vertical speed of the profiler is much greater than the surface wave-induced orbital velocities. However, vertical profiling is inefficient for obtaining large sample sets of turbulence statistics in the near-surface region due to the large changes of the turbulent statistics as a function of depth. It is also difficult to detect and adequately measure regions of large horizontal gradients. Towed methods can efficiently generate large sample sets of dissipation estimates but then are typically degraded by broadband motion contamination due to the nonstationary push–pull motion of these devices. The measurements are also affected by the large area of influence of the ship's wake. Bow- or submarine-mounted devices can also efficiently produce large sample sets. As with all other approaches, measurements from the bow- or submarine-mounted devices offer unique challenges. For example, to obtain meaningful data from these types of systems, ship motion-induced effects must be assessed and minimized.

This paper describes the new bow-mounted system developed for TOGA COARE to study microstructure and turbulence in the upper meters of the ocean. The purpose of the paper is to document the sensors characteristics and processing algorithms, to support future papers that will address analysis of the near-surface measurements collected during TOGA COARE. The high speed of the measurements (5–10 kt) produces scale separation between the wave-induced velocity field and turbulence and allows transformation to the spatial domain for the estimation of turbulence statistics. As is demonstrated in this paper, vibration contamination for the bow-mounted system deployed during the COARE experiments is limited to narrow frequency bands. The ship motion induced by the surface wave field produces scans of the near-surface layer. Depth variation due to ship motion can be sorted out using a high-resolution pressure device.

Section 2 outlines the techniques and instrumentation for small-scale measurements from the bow of the vessel. Section 3 presents calibrations of the sensors, sensor response functions, and noise spectra. Section 4 describes the processing algorithms, including the approach to detect surface penetration and contamination by air bubbles. Section 5 presents examples of the data collected during TOGA COARE. Section 6 is the summary.

2. Instrumentation and techniques

For the TOGA COARE project, we developed two configurations of the bow sensor system. The first configuration was used during the COARE IOP-3 and EQ-2 legs of the R/V *Moana Wave* in January to March 1993. This paper describes the second configuration of the bow sensor system that was used during the COARE MW9410 and EQ-3 legs of the R/V *Moana Wave* in March to May 1994. A more detailed description of both modifications is in Soloviev et al. (1995).

The probes were originally designed in ''Granit'' (St. Petersburg, Russia) for microstructure and turbulence measurements within the depth range of 0–500 m. They included conductivity, temperature, and electromagnetic velocity probes and their associated electronics. For the TOGA COARE project, pressure and acceleration sensors were added to the bow probes. A photograph of the bow probes is shown in Fig. 1a. The device on the left is the electrical conductivity, temperature, and pres-

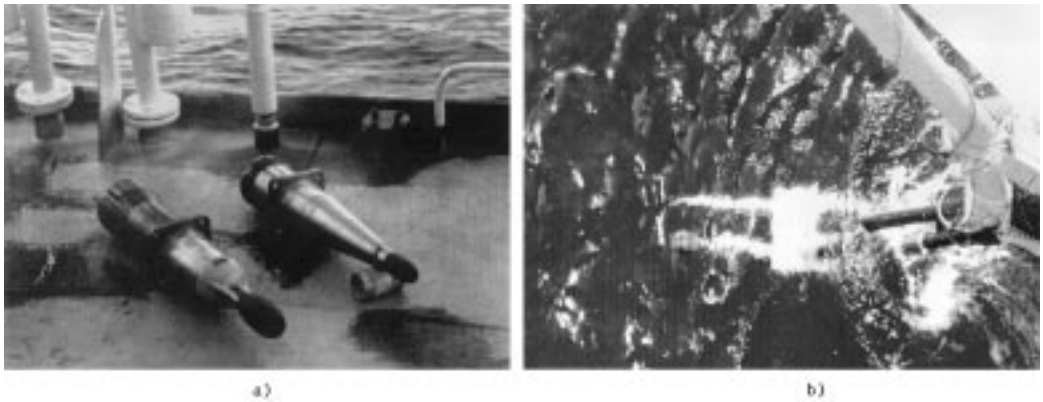

FIG. 1. Bow probes photograph: (a) on the deck and (b) mounted on the bow of *Moana Wave.*

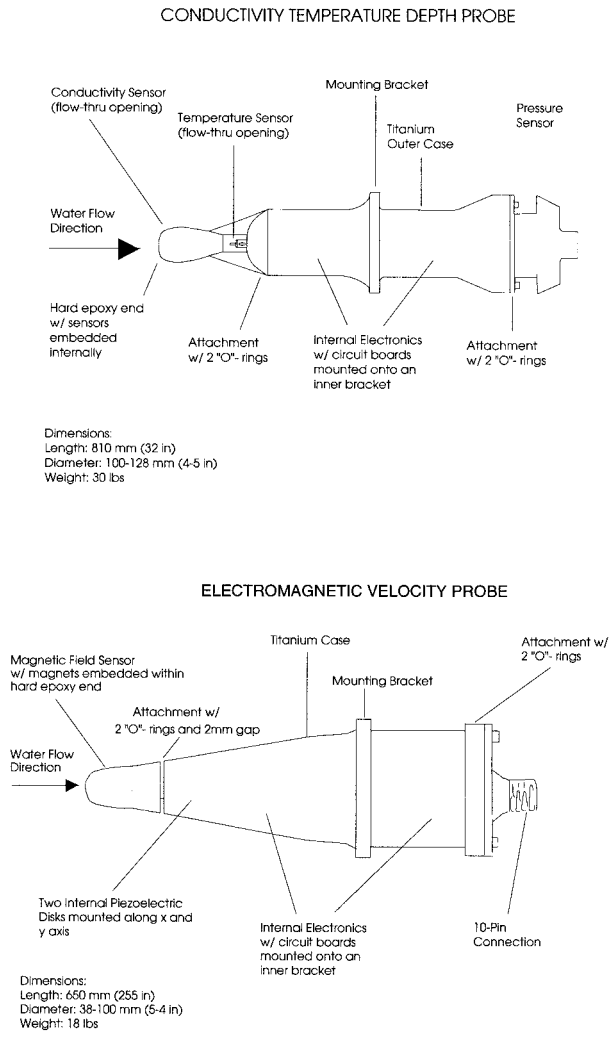

FIG. 2. Schematic construction of the bow probes.

sure (ECTP) probe; the device on the right is the electromagnetic velocity and acceleration (EMVA) probe. The bodies of the probes are made from titanium. Diagrams of the construction of the ECTP (top) and EMVA (bottom) probes are shown in Fig. 2. The mechanical characteristics of the bow probes are in Table 1. The bow probes have a functional control (FC) mode that is intended for checking normal operation of the electronics of the probes. Table 2 gives the ECTP probes' main technical characteristics for the different COARE cruises. A special metal frame was designed to install the probes in an undisturbed region ahead of the moving vessel. Figure 1b is a photograph of the bow probes mounted on the *Moana Wave.*

a. Conductivity and temperature (ECTP) probe

1) CONDUCTIVITY SENSOR

The conductivity probe consists of a conductivity cell (of the throughflow type) and its associated electronics. A diagram of the conductivity cell is in Fig. 3b. This inductive sensor consists of two coaxial toroid inductors. In a conductive medium, an inductive conductivity cell has an isolated ''conductivity loop'' composed of two inductors. A 16-kHz ac voltage is applied to the primary voltage inductor, which induces current into the ''conductivity loop'' (seawater). The secondary current inductor converts the current from the conductivity loop into an output voltage of the conductivity cell. The value of the current in the conductivity loop depends on the conductivity of the water. The output ac voltage is amplified and then rectified into the dc signal by the electronic circuits. An important advantage of inductive

TABLE 1. Mechanical characteristics of bow probes.

Maximum speed of water flow	25 kt
Lifetime	10 yr
Resource	15 000 h
Weight (ECTP)	15 kg
Weight (EMVA)	12 kg

TABLE 2. Main technical characteristics of ECTP probes.

Cruise on R/V *Moana Wave*	COARE IOP-3 EQ-2	COARE MW9410	COARE EQ-3
Parameter	ECTP #A283	ECTP #1	ECTP #1
Temperature			
Range (°C)	−2–35	14–34	14–34
Accuracy (°C)	<0.1	<0.1	<0.1
Stability during 8 h (°C)	<0.01	<0.01	<0.01
Digital resolution (°C)	0.003	0.005	0.005
Response time of primary sensor (ms)	35	35	35
Fluctuation temperature			
Range (°C)	+2.5	±1.0	±1.0 (±2.0 from 11 Apr 94)
Noise level (°C)	0.001	0.001	0.001
Digital resolution (°C)	0.0012	0.0005	0.0005 (0.001 from 11 Apr 94)
Frequency range (Hz)	0.012–50	0.012–50	0.012–50
Amplification factor, A_f	25	10	10
Conductivity			
Range (S m^{-1})	1.5–7.0	3.1–6.1	3.1–6.1
Accuracy (S m^{-1})	<0.01	<0.01	<0.01
Stability during 8 h (S m^{-1})	<0.001	<0.001	<0.001
Digital resolution (S m^{-1})	0.00056	0.0012	0.0012
Spatial resolution (m)	0.1	0.1	0.1
Fluctuation–conductivity			
Range (S m^{-1})	±2.5	±0.1	±0.1 (±0.2 from 11 Apr 94)
Digital resolution (S m^{-1})	0.00012	0.00005	0.00005 (0.0001 from 11 Apr 94)
Noise level of output voltage (S m^{-1})	0.0001	0.0001	0.0001
Frequency range (Hz)	0.012–50	0.012–50	0.012–50
Amplification factor, A_f	50	25	25
Pressure			
Range (db)	0–25	0–25	0–25
Accuracy* (db)	0.1	0.1	0.1
Digital resolution (db)	0.01	0.01	0.001

* After correction for temperature dependence.

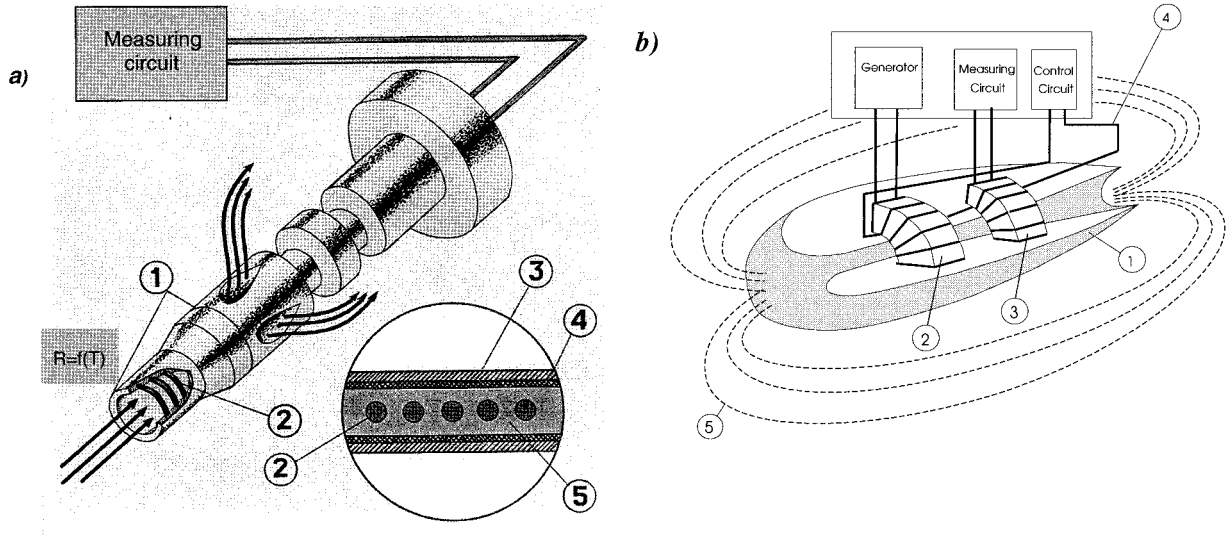

FIG. 3. (a) Construction of the primary temperature sensor: 1) the locations of laser welds, 2) the copper microwire of 20-μm diameter, 3) titanium body with 100-μm-thick walls, 4) isolation cover by nitride of silicon, and 5) compound filling. The balloon shows a cross section of the sensitive element wall in more detail. (b) Theoretical field of the inductive conductivity cell: 1) the epoxy body of the cell, 2) voltage transformer, 3) current transformer, 4) control winding, and 5) the ''conducting loop.''

conductivity cells is that biological growth on its exposed surfaces does not substantially interfere with the conductivity measurement. Also, because no electrodes directly contact seawater, there is no electrical polarization.

2) Temperature sensor

The temperature probe consists of a primary temperature sensor (of the throughflow type) and its associated electronics. The primary temperature sensor is made of copper wires placed between two thin-walled (100 μm) titanium cylinders (Fig. 3a) that are welded together using a laser welding technique. This construction provides a hermetic seal for protection of the microwire from the seawater. Using pure copper as the material for the primary temperature sensor provides a good linearity of the probe in a wide temperature range ($-2°$–$+35°$C). The small diameter of microwire and thin-walled cylinders (especially the internal cylinder on which the microwire is wound) provides a response time of the temperature sensor of 35 ms for water-flow speeds greater than 3 m s^{-1}. The internal surfaces of the cylinders are covered by insulation, nitride of silicon, to provide isolation of the microwire from the internal and external cylinders. A filler compound between cylinders is used to decrease the influence of wire strain caused by environmental effects. Constructionally, the temperature sensor is installed behind the throughflow conductivity cell. The conductivity cell protects the temperature sensor from mechanical damages. However, the body of the conductivity cell disturbs the flow. The response time of the temperature sensor thus depends on the water-flow speed and only asymptotes to the inherent response of the microwire at speeds greater than 3 m s^{-1}.

3) Fluctuation temperature and conductivity channels

There are also fluctuation temperature and fluctuation conductivity channels in the ECTP probe. The fluctuation channels are derived from the temperature and conductivity sensors. They are processed differently than the dc temperature and conductivity channels to emphasize higher frequencies. The fluctuation channels are bandpass filtered in the frequency range of 0.012–50 Hz, followed by additional amplification. The fluctuation channels have a substantially lower digitizing noise level than the dc channels because of the additional amplification factors (A_f) shown in Table 2 and because the high pass reduces the dynamic range and hence the least significant bit of the digitizer. The fluctuation channels are used for microstructure statistics, whereas the mean temperature and conductivity channels are used for salinity and density calculations. Originally, the fluctuation channels in the ECTP probe were constructed to increase the dynamical range of the device for analog transfer of the signals to the data acquisition system. The fluctuation channels are also used to detect possible external electrical disturbances on the temperature and conductivity channels during the transmission of the analog signals to the data acquisition system. After mean and fluctuation signals are converted into the physical units, the real signals should be consistent in the frequency range of 0.012–50 Hz with each other. The electrical disturbances picked up on the line between sensors and data acquisition system should be a factor of A_f weaker on the fluctuation channel compared to the mean channel. The amplification factor A_f is equal to 25 or 10 for the fluctuation temperature and 50 or 25 for the fluctuation conductivity channel (see Table 2).

4) Pressure

For the COARE expedition, the strain-gauge pressure sensors (serial type D) produced by the Prompribor Plant (Orel, Russia) were added to the ECTP probes. The pressure sensor is installed in the tail section of the ECTP probe.

b. Electromagnetic velocity and acceleration (EMVA) probe

The EMVA probe consists of a three-component fluctuation velocity vector and vibrational-acceleration sensor(s).

1) Fluctuation velocity sensor

The fluctuation velocity sensor generates signals proportional to the longitudinal, transverse, and vertical components of the fluctuation velocity vector, which appear at the output of the low-frequency amplifiers. The operation of the sensor is based on the principle of electromagnetic induction. In the area of interaction of the flow (V) of the conducting water and magnetic field (B), an electrical field E is induced with the appropriate distribution of the electric potential (φ). Potential differences between the two points of the interaction area are determined by directions of the vectors **V** and **B** and are proportional to the product of their moduli (Fig. 4).

The primary sensor is made of dielectric material (an epoxy compound) in the form of a rotation body (Fig. 4a). Four permanent magnets are shaped according to the form of the dielectric body. The magnets are placed symmetrically with respect to the nose of the sensor (Fig. 4b). Four measuring platinum electrodes coated with platinum black are placed symmetrically within lines of the dielectric body with respect to the nose of the sensor. Electrodes are placed at the centers of the magnetic gaps. The exposed tips of the electrodes are polished to the surface of the dielectric body.

The coordinate system with respect to the measured fluctuation velocity vector (Fig. 4c) is determined by

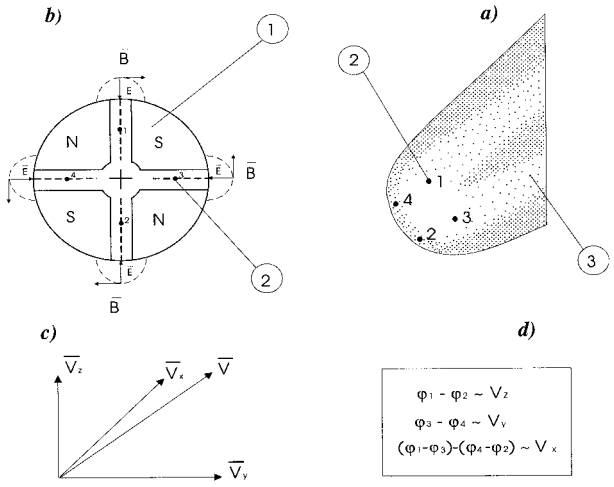

FIG. 4. Three-component fluctuation velocity sensor: (a) view of dielectric body and electrode locations; (b) cross-sectional view of the location of the magnets (1), electrodes (2), and the geometry of the **E**, **V**, and **B** fields; (c) fluctuation velocity coordinate system with respect to orientation of the sensor view shown in (a); and (d) the relationships between electrode voltage outputs and fluctuating velocity components.

the position of the magnetic gaps. The potential differences between the measuring electrodes are proportional to orthogonal components of the fluctuation velocity vector (Fig. 4d).

In contrast to traditional internal-flow electromagnetic sensors, this sensor exploits an external part of the magnetic field. The potential field is formed only by the part of the magnetic field that emerges beyond the limits of the magnetic gap. The use of the external part of the magnetic field improves the hydrodynamic form of the primary sensor, as shown in Fig. 4. The main technical characteristics of the fluctuation velocity probes are in Table 3.

2) ACCELERATION SENSORS

The acceleration sensors measure vibrational accelerations of the EMVA probe. Three types of acceleration sensors were used in different legs. The technical specifications for each sensor are listed in Table 4. For the EQ-3 cruise acceleration sensor ''ICSensors'' (model 3145) was used. The model 3145 is a precision accelerometer intended for instrumentation applications. The module consists of a silicon micromachined accelerometer, amplification, signal conditioning, and temperature compensation from $-20°$ to $+85°$C. A single supply is required, and full-scale output is ± 2 V about a 2.5 V offset. It is designed with built-in damping, thereby allowing a wide usable bandwidth. In addition, the accelerometer element is protected from shock by overrange stops in the silicon microstructure. The lightweight Valox™ housing provides easy attachment to the measurement surface. A detailed calibration sheet that provides the measured test and calibration data for the sensor is included with each unit.

c. Deck connector, electrical cables, and lab unit

Analog signals are transmitted to the data acquisition system in the lab of the ship by an approximately 50-m-length, waterproof, shielded conducting cable. This cable is also used to provide a ± 20-V power supply to the bow sensors from the lab source, signal return wire, and power ground. A deck connector junction box is used to join the two underwater cables from the ECTP and EMVT into a single deck cable. The junction box and the cables are hermetically constructed to ensure waterproof integrity. A deck unit is used for anti-alias low-pass filtering of the signals from the bow probes prior to transmitting to the recording system. The cutoff frequency of the filters was set up equal to or one-third lower than the sampling rate. The deck unit also supplies

TABLE 3. Main technical characteristics of EMVA probes.

Cruise on the R/V *Moana Wave*	COARE IOP-3 COARE EQ-2	COARE MW9410	COARE EQ-3
Parameters	EMVA #465	EMVA #2	EMVA #1
Longitudinal fluctuation velocity (V_x)			
Range (m s^{-1})	± 2.3	± 2.5	± 2.5
Precision (%)	<5	<5	<5
Digital resolution (m s^{-1})	0.0011	0.0011	0.0011
Frequency range (Hz)	0.05–600	0.05–200	0.05–200
Transversal fluctuation velocity (V_y)			
Range (m s^{-1})	± 2.8	± 5	± 5
Precision (%)	<5	<5	<5
Digital resolution (m s^{-1})	0.0014	0.0022	0.0022
Frequency range (Hz)	0.05–600	0.05–200	0.05–200
Vertical fluctuation velocity (V_z)			
Range (m s^{-1})	± 2.8	± 5	± 5
Precision (%)	<5	<5	<5
Digital resolution (m s^{-1})	0.0014	0.0022	0.0022
Frequency range (Hz)	0.05–600	0.05–200	0.05–200

TABLE 4. Vibrational acceleration sensors installed on EMVA.

Cruise on the R/V *Moana Wave*	COARE IOP-3/ COARE EQ-2	COARE MW9410	COARE EQ-3
Parameter	EMVA #465	EMVA #2	EMVA #1
Type of vibration sensors	Krylov's Institute, St. Petersburg, Russia (type VP-7)	"Brüel and Kjæ" (damper problem was detected)	"ICSensors" (type 3145)
Measured components	g_x	g_x	g_x, g_z
Range (m s^{-2})	±10	±10	±25
Precision (%)	2	5 (within the range ±6 m s^{-2})	0.2
Frequency range (Hz)	1–900	0.5–200	0–200

power to the bow probes and initiates a functional control mode (FC).

After installation of the probes on the bow of the vessel, an additional dc bias occurs for the conductivity channel because the conductivity probe is mounted relatively close to the metal body of the vessel and bow frame. The electrical field of the conductivity cell attenuates strongly out of its approximately 10-cm sensitive area. However, the massive metal parts of the bow construction (conductivity of which is much higher than of the seawater) result in some dc bias on the conductivity channel. It is equivalent to a shift of the calibration of $\Delta C = 0.05$ S m^{-1}. This shift corresponds to a 0.9% change in the conductivity cell constant. This constant bias was corrected during data processing.

d. Data acquisition

The data were acquired in digital form by the National Instruments' data acquisition board (AT-MIO-16, 12 bit, 40 000 samples per second) with a Dell 486 computer. An acquisition program provided the possibility of selecting any individual record time length with 9 or 10 channels. Typically, an individual record length of 10 min was used, with no gaps between the individual 10-min segments. Data were acquired at two sampling rates: 400 and 40 Hz. The records were usually made in series. Data were transmitted simultaneously to the Dell PC and to a Sun Microsystems Workstation and stored on hard disks. Real-time processing of turbulence parameters was available to help provide selective sampling of regions.

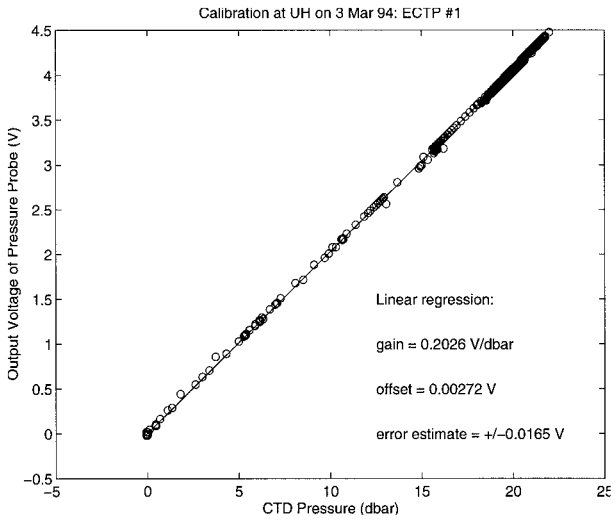

FIG. 5. Calibration of pressure sensor of ECTP #1. Error estimates correspond to 50% confidence interval.

3. Calibrations and bench tests

Calibrations and tests were performed with the power supply, anti-aliasing filters, and electrical cables that were used during field measurements.

a. ECTP

Precruise calibration of the pressure sensor, including temperature dependence, was made at the University of Hawaii. Figure 5 shows the calibration characteristics of the pressure sensor of ECTP#1. Temperature dependence of the pressure sensor was determined to be equal to −0.04 db °C^{-1}. To reduce the influence of the temperature dependence, the pressure at 0 m was corrected each time the bow sensors surfaced into the air.

Precruise calibration of the temperature and conductivity probes was done in Granit using a temperature-controlled water bath with precision thermostat TWP-6 with a certified accuracy of 0.005°C. Water temperature was measured by two mercury thermometers with accuracies of 0.01° and 0.1°C. Conductivity was measured by conductometer CL4 (produced in Russia) with a rated accuracy of 0.25%. TWP-6, CL4, and mercury thermometers were annually tested by the D. I. Mendeleev's Institute of Metrology (St. Petersburg, Russia).

After transporting the devices from Granit, the temperature probes were tested at the University of Hawaii during March 1994. The ECTP probes and a reference temperature probe, Sea-Bird Electronics SBE-3, were placed in a well-circulated water tank. The water was cooled down with ice, then left to warm naturally. This resulted in some hysteresis of the calibration dependencies caused by the large thermal mass of the titanium bow probe. The objective of the test done at the University of Hawaii was to check the probes functionally

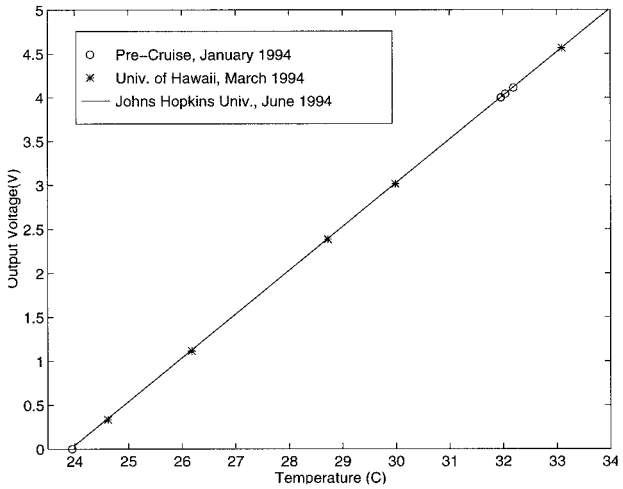

FIG. 6. Comparison of temperature calibrations and tests of ECTP #1; ''o'' denotes the calibration points obtained in Granit by thermometer with 0.01°C accuracy; ''*'' denotes the points obtained during testing at the University of Hawaii; straight line is the regression estimated by JHU/APL from the JHU/APL calibration data.

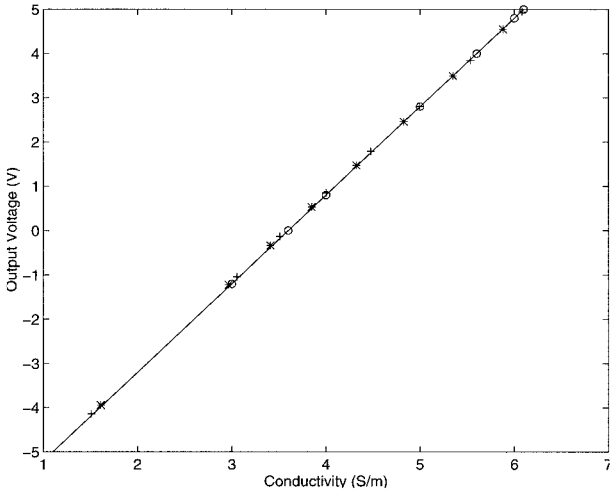

FIG. 7. Comparison of conductivity calibrations for ECTP #1 made in Granit and at JHU/APL; ''○'' denotes calibration points obtained in Granit; the straight line is their regression. ''*'' and ''+'' denotes calibration points measured by JHU/APL on 19 and 23 May 1995, respectively.

before the field work and to verify that the bow sensors were not damaged during transportation.

The postcruise calibration of ECTP#1 was done at The Johns Hopkins University Applied Physics Laboratory (JHU/APL) on 19 May 1994. The calibrations are based on a temperature-controlled circulating water bath that uses National Institute of Standards and Technology standards for temperature and salinity. The circulating bath has spatial temperature stability to within ±0.2 m°C. A Neil Brown Instrument Systems' Model CT-2 Conductivity and Temperature Standard provides the reference conductivity and temperature values. The CT-2 temperature accuracy over the range from 0° to 30°C is checked against the triple point of water at 0.01°C and the melting point of gallium at 29.7717°C. The conductivity accuracy over the range from 2.8 to 6.4 S m^{-1} is checked against the salinity of standard seawater. The CT-2 sensor has calibration accuracies of ±1 m°C and ±0.0002 S m^{-1} for temperature and conductivity, respectively. The calibration of ECPT #1 covered a range from 5.4° to 35°C and 0.66 to 6.4 S m^{-1}. Figure 6 compares all available temperature calibrations and tests of ECTP #1 with the JHU/APL calibration. The precruise calibrations agree within the 95% confidence interval of the postcruise calibrations done at JHU/APL. The maximum difference between these calibrations is 0.02°C in the COARE range of surface temperatures (24°–34°C).

Figure 7 compares the pre- and postcalibrations of conductivity sensor of ECTP #1. Only points within a linear range of the output voltage (±5 V) were used. The calibrations display good agreement. The maximum difference between the calibrations from Granit and JHU/APL, within the range of conductivity in the near-surface layer of the ocean in the COARE domain (5.1–6.1 S m^{-1}), is equivalent to 0.0038 S m^{-1}. Table 5 compares pre- and postcalibrations of the temperature and conductivity for ECTP #1.

The response time of the temperature sensor was determined using data from a free-rising profiler with the same type of temperature sensor as well as a 3-ms response cold-film thermoanemometer (DISA). The measuring cycle of the free-rising profiler included the descent of the device into the water, positioning at a prescribed depth, and then the collection of data in the vertically oriented rising regime. Details of these measurements are in Soloviev et al. (1995). The conductivity signal was an indicator of intersection of the air–water interface. The speed of the profiler at the initial air–sea intersection was greater than 3 m s^{-1}. When the temperature sensors were immersed in the ocean they started to observe a water temperature that was about 2°C dif-

TABLE 5. Comparison of ECTP #1 calibrations.

Place	Date 1994	Calibration	Sensor	Gain	Offset	Rms error of fit	Range
Granit	Jan	Precruise	T	0.4992 V/°C	−11.956 V	0.0039°C	24°–34°C
JHU/APL	May	Postcruise	T	0.4956 V/°C	−11.805 V	0.0015°C	24°–34°C
Granit	Jan	Precruise	C	2.00 V/(S m^{-1})	−7.20 V	0.0011 S m^{-1}	5.1–6.1 S m^{-1}
JHU/APL	May	Postcruise	C	1.98 V/(S m^{-1})	−7.094 V	0.0018 S m^{-1}	5.1–6.1 S m^{-1}

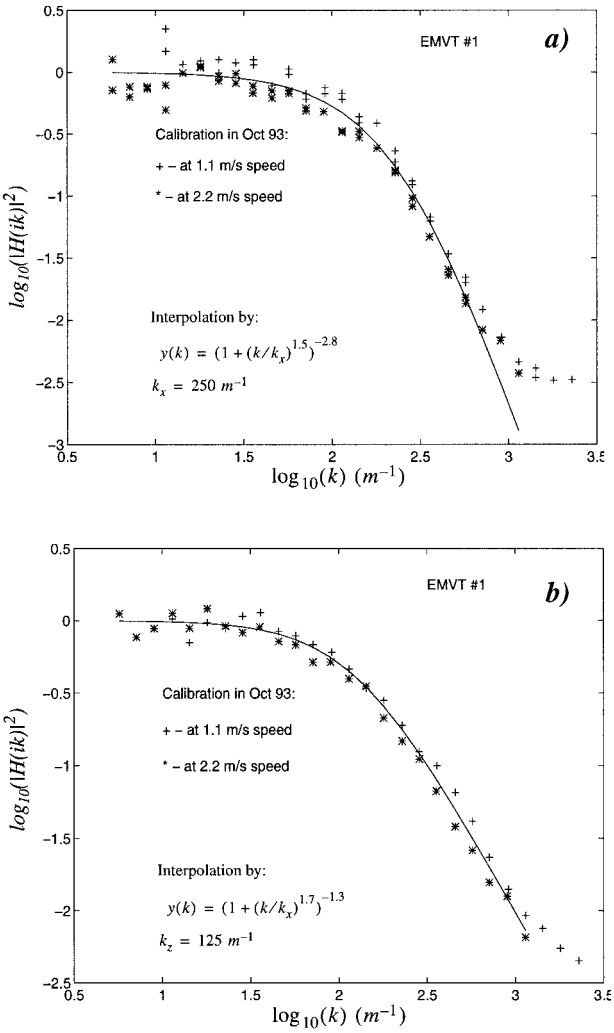

FIG. 8. Spatial response for (a) V_x and (b) V_z channels. Here $|H(ik)|$ is the wavenumber response-function magnitude, k is the radian wavenumber ($k = 2\pi/\lambda$, where λ is the wavelength in meters per cycle), and $i^2 = -1$.

ferent from the air temperature. This transitional process provided an estimate of the response. The temporal lag of the regular temperature sensor was determined to be 35 ms.

b. EMVA

The precruise calibration of the fluctuation velocity probes was done in Granit using two mean speeds of a turbulent jet, 1.1 and 2.2 m s^{-1}. The test was made at facility HDF-FJ, which is a water tank with submerged flow. The jet emerges from a 60-mm-diameter nozzle converging with the flow. The initial diameter of the pipe is 100 mm. The probe to be calibrated is placed in the region of developed turbulence at a distance of 10 diameters of the nozzle along the axis line of the jet. Characteristics of the mean flow were determined using the Pitot tubes annually calibrated by the D. I. Mendellev's Institute of Metrology. The fluctuation characteristics of the flow had been known from measurements at the two flow speeds, 1.1 and 2.2 m s^{-1}, by a hot-film thermoanemometer DISA 55D01 with sensor 55A87. Calibration of the thermoanemometer was done at the same facility but in the region of minimal fluctuation velocities (0.5%) near the face of the nozzle. An HP 8064 spectrum analyzer was used for spectral analysis of the signals. The absolute accuracy of estimating the gain using this technique was only about 20%. At the same time, the estimate of the response function of the velocity sensors is expected to be within 5% accuracy because the response function does not depend on the absolute calibration of the flow.

TABLE 6. Postcruise calibration of fluctuation–velocity probes (EMVA) at JHU/APL.

EMVA	Gain	Precision of calibration
#1	3.33 V m^{-1} s	3%
#2	4.57 V m^{-1} s	3%

Figures 8a and 8b show the results of measurements of the wavenumber response function magnitude $|H(ik)|$ of EMVA #1 in Granit at 1.1 and 2.2 m s^{-1} flow speeds, respectively. Here, $H(ik)$ represents the spatial response of the sensor on a small scale; $|H(ik)|$ is defined by

$$|H(ik)|^2 = E_m(k)/E_r(k), \tag{1}$$

where k is the wavenumber (rad m^{-1}), E_m is the wavenumber spectrum measured by the tested sensor, and E_r is the wavenumber spectrum measured by the reference velocity sensor. The wavenumber spectrum $E(k)$ is derived from the measured frequency spectra $S(f)$ using G. T. Taylor's hypothesis of ''frozen turbulence'' by the following well-known formulas:

$$k = 2\pi f/U_0$$

and

$$E(k) = S(f)U_0/(2\pi), \tag{2}$$

where f is the frequency (Hz) and U_0 is the relative flow speed.

At wavenumbers exceeding 500 m^{-1} [$\log_{10}(500) = 2.7$], the spectrum is dominated by sensor noise (Fig. 8). Curves (shown in the figures) were visually fit to the measured transfer functions. These interpolated transfer functions are used to correct the turbulence spectra in high wavenumber range.

A standard gain, 4.0 V (m s^{-1})$^{-1}$, for the V_x(longitudinal) fluctuation velocity channel for both EMVT#1 and EMVT#2 probes was installed in Granit; the accuracy of the available fluctuation velocity testing equipment was 20%. Estimation of the gain factor for the V_x fluctuation velocity channel was done at JHU/APL (Table 6). The V_x channel was dynamically calibrated by oscillating the sensor longitudinally in the

presence of a mean flow in the JHU/APL flow channel. Each calibration run lasts for 30 min. The sensor traverses a distance of $\pm 2R$ ($R = 2.54$ cm) during an oscillation period. The oscillation generates a sinusoidal output, resulting in a spectral peak approximately two orders of magnitude above the spectrum due to the background flow. The frequency of the oscillation, ω_0 (rad s^{-1}), is estimated from the location of the spectral peak, and the amplitude, A (V), is estimated by integrating the spectral peak. The peak speed of the translation velocity is $\pm R\omega_0$ and the gain factor V $(m\ s^{-1})^{-1}$ is $A/R\omega_0$. The mean speed was 0.5 m s^{-1}, and the sensor was oscillated at 0.4 Hz or at a speed of 0.064 m s^{-1}. The combined flow velocity and sensor velocity therefore is 0.5 ± 0.064 m^{-1}. This method uses only the mean speed to determine what oscillation frequency to select. The oscillation frequency is selected such that the peak oscillation speed is typically 10%–15% of the mean flow speed. The method does not require accurate knowledge of the mean flow speed. The accuracy, limited only by the accuracy of the estimates of the oscillation frequency and the amplitude (derived from integration of the spectral peak), is estimated to be approximately $\pm 3\%$. The calibrations made at JHU/APL differ from the Granit calibrations by -17% and 14% for probes #1 and #2, respectively. This is within the 20% accuracy of the testing equipment for the fluctuation velocity that is used in Granit for adjustment of the gain to the standard value, 4.0 V $(m\ s^{-1})^{-1}$.

Calibration of the acceleration sensors ''ICSensors'' (Model 3145) was taken from their technical description.

4. Processing the signals

a. Pressure-to-depth conversion

To accurately maintain a coordinate system fixed to the surface, the pressure is corrected by the amount the pressure sensor reads when the probe surfaces, thereby zeroing it in the air. Each time the probe surfaces this correction changes. Between surface events the previous value is used. Penetration of the surface is determined from the conductivity signal.

The dynamical pressure is a complicating factor in the pressure-to-depth conversion. The pressure signal is $P = P_d + P_h$. The hydrostatic component P_h is used to calculate the depth of the probe. The dynamical component P_d depends on the relative flow and on the location of the pressure sensor. The orbital velocities of the surface waves and the ship's pitching produce fluctuations of the relative flow that affect the dynamical pressure. To reduce the influence of the dynamical component, the pressure sensor is installed in the tail section of the ECTP probe.

The 0.6-m horizontal separation between the conductivity cell and the pressure sensor results in some additional uncertainty in relative positions of the sensors with respect to the air–sea interface at the probes' surfacing. The total rms uncertainty in pressure-to-depth conversion for the bow measurements is estimated by Soloviev and Lukas (1996) as being between 0.02 and 0.1 db.

b. Temperature and conductivity

The bow probes collect data in the near-surface layer of the ocean, sometimes surfacing or encountering water with air bubbles. There are also many electromagnetic sources on the ship that sometimes produce influences on the electrical circuits. Algorithms have been developed at the University of Hawaii to detect and remove these sections from the signals. The temperature and conductivity processing flowchart are shown in Fig. 9.

The conductivity channel is a good indicator for detecting when the probe surfaces because a change of conductivity signal at the intersection of the air–sea interface is by several orders of magnitude more than the natural conductivity fluctuations in seawater. This program first locates data segments in which conductivity C is lower than 4.6 S m^{-1}. Next, it finds the beginning and ending points where the record is disturbed. For this purpose the salinity difference is analyzed. The first point in the backward direction where the difference becomes equal to zero and the first point in the forward direction where the difference becomes equal to zero are determined. Then 0.1 s prior to the first point and 0.9 s after the second point are identified as the beginning and ending points of the segment that is to be removed. After returning to water the conductivity cell retains some air inside it. It takes time for the air bubbles to dislodge from the cell, which is why the number of points removed before and after surfacing is different. Predicting the time interval when the conductivity signal still contains air bubbles is difficult, as it depends on the wind–wave conditions in addition to the ship speed and direction with respect to the waves. Due to the unpredictable nature of this time interval, after removing the out-of-water data, spikes of a negative direction are sometimes still present on the conductivity signal segments next to the removed areas. The areas next to the surfacing are examined for points where the salinity differences are negative. These points are then removed to the point where the salinity difference first becomes positive. The standard deviation is calculated on the whole 10-min file after removing segments that were out of the water. Segments of the salinity records where the difference is more than five standard deviations are eliminated.

The temperature-sensitive element is smaller in size than the conductivity cell and is located on the axis line of the conductivity cell. The temperature-sensitive element intersects the ocean–air interface when half of the conductivity cell is in the air. The processing program removes out-of-water temperature data from when

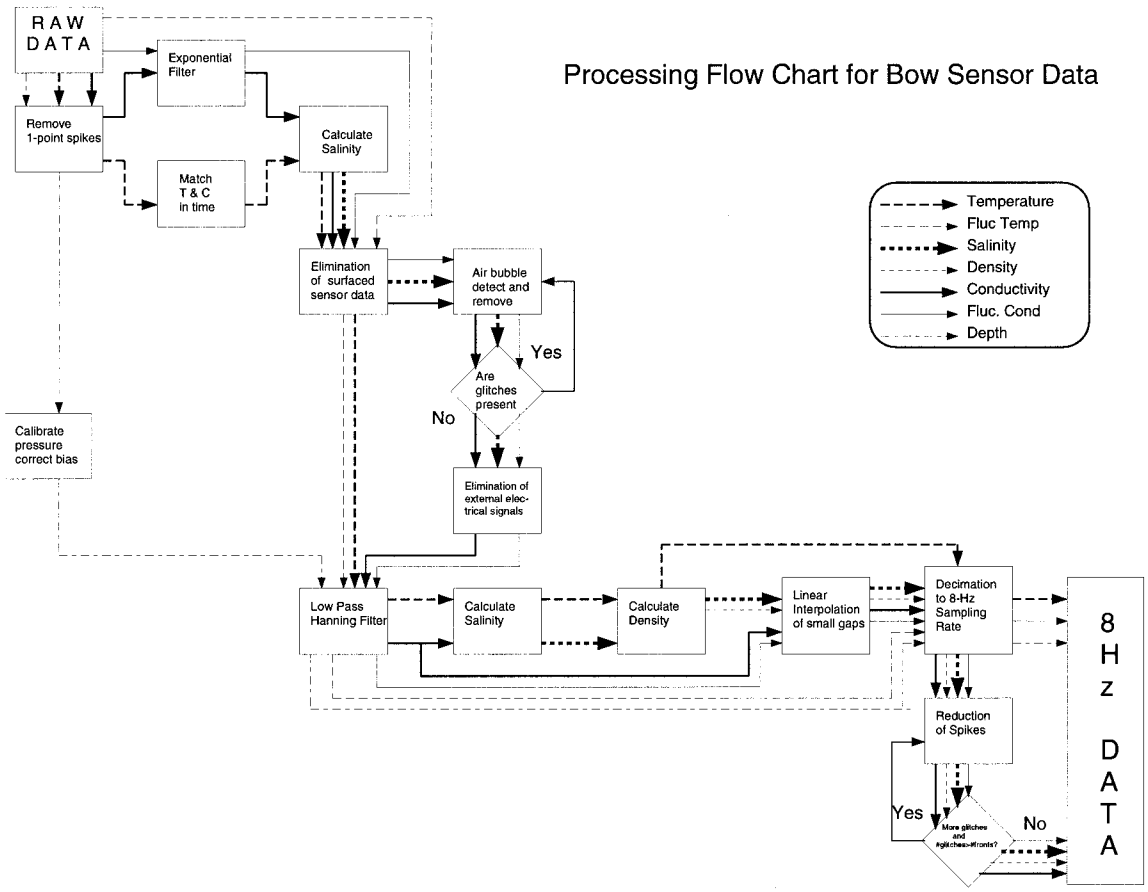

FIG. 9. Temperature and conductivity processing flowchart.

the conductivity is less than 4.6 S m^{-1} until the last time conductivity is less than 4.6 S m^{-1}.

External electrical noise (generated from equipment on the ship) is detected by comparing the signals on T and C with the corresponding signals on the fluctuation channels T' and C'. The fluctuation channels represent T and C signals processed by an analog high-pass frequency filter with a cutoff frequency of 0.012 Hz and are amplified prior to transferring to the lab for analog-to-digitial conversion. When the mean and fluctuation channels are compared on the same temperature and conductivity scale, useful signals coincide in the frequency domain that is greater than 0.012 Hz, but the amplitude of any external electrical noise differs by a factor of 25 or 10 times for temperature and 50 or 25 times for conductivity; see section 2a(3). During the almost 1-month record in the EQ-3 cruise, only several cases of external electrical noise contamination were detected.

To compensate for the temperature and conductivity sensors' spatial separation of $L = 8.4$ cm, conductivity is lagged by the amount of time $\Delta t = L/U_0$ it takes water to travel that distance, which varies with different ship speeds U_0. To match the response time of the temperature and conductivity signals before calculating salinity, the conductivity channels are processed by an exponential filter (Fozdar et al. 1985) with a cutoff frequency of 4.547 Hz, which corresponds to the 35-ms response time of the temperature sensor (1.1 m for a ship's speed of 5 m s^{-1}).

A second filter is applied to both temperature and conductivity to remove high-frequency noise on the temperature channel and to maintain the temporal match between temperature and conductivity induced by the 4.547-Hz exponential filter. This is a Hanning filter with a cutoff frequency of 4 Hz and a window length of 8 points for 40 Hz and 81 points for 400-Hz data. This filter also reduces the impact of mismatch between temperature and conductivity by reducing the energy in both channels at frequencies greater than 4 Hz. Salinity and density, σ_θ, are computed using standard UNESCO routines. To reduce the results of a T and C mismatch due to a residual difference in response time, which can induce salinity spikes, and to avoid aliasing when decimating the time series, the salinity signal is additionally processed by a low-pass Hanning filter with a cutoff frequency of 4 Hz that corresponds to smoothing the salinity over 1.25 m in the horizontal direction for a ship speed of 5 m s^{-1}. Note that gaps smaller than 0.6s

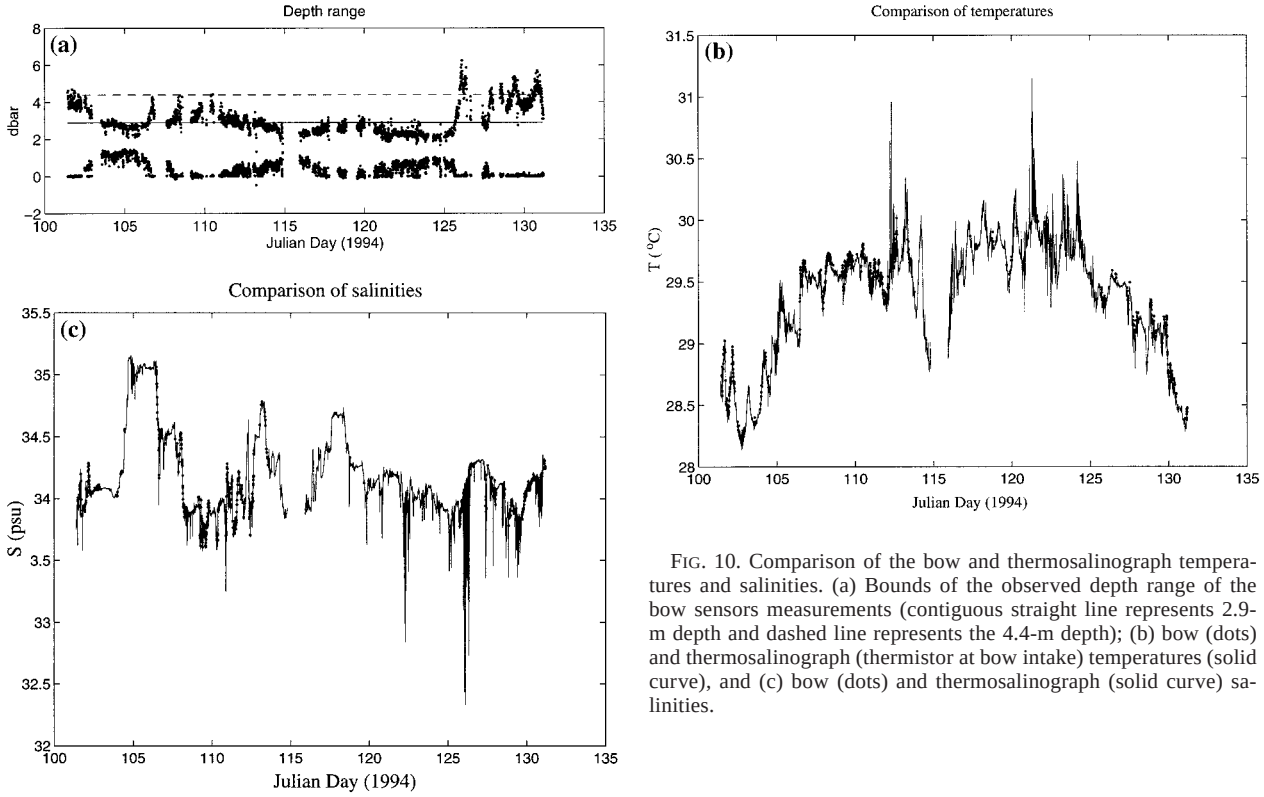

FIG. 10. Comparison of the bow and thermosalinograph temperatures and salinities. (a) Bounds of the observed depth range of the bow sensors measurements (contiguous straight line represents 2.9-m depth and dashed line represents the 4.4-m depth); (b) bow (dots) and thermosalinograph (thermistor at bow intake) temperatures (solid curve), and (c) bow (dots) and thermosalinograph (solid curve) salinities.

long (24 points at 40 Hz or 240 points at 400 Hz) are filled using linear interpolation.

c. *Combining the bow sensors and the thermosalinograph system*

On the *Moana Wave*, there is a thermosalinograph system that collects water from 3 m below the waterline and pumps it onboard the vessel to a Sea-Bird Electronics (SBE-21) CTD (Shinoda et al. 1995). The accuracy of the SBE-21 was 0.01°C per 6 months and 0.001 S m^{-1} per month. Figures 10b and 10c compare the bow and thermosalinograph temperatures and salinities. The bow sensor temperature and salinity data are averaged in 10-min segments within the depth range from 2.9 to 3.1 m and are represented by points. The depth range of the bow sensors depends on the surface waves and on the ship's speed and direction. Figure 10a shows the full range of depths observed during the *Moana Wave* EQ-3 cruise. If strong pitching motions of the vessel occur the thermosalinograph intake (at 3 m) can entrain air bubbles. These air bubbles produce negative spikes in the conductivity signal. For this reason the comparison excludes cases in which the maximum depth of the bow sensors was over 4.4 m, as well as below 3.1 m. The first 10-min segments at the beginning of each series were removed from the comparison if the time interval between records was more than 20 min. This is because in some cases the power supply was switched off, and it takes about 10 min to equilibrate the electronics after switching on the electrical supply.

The differences in temperature and salinity between the bow sensors and thermosalinograph were interpolated by second-order polynomials. For the temperature there was a constant offset of 0.034°C at the beginning of the cruise and 0.057°C at the end, with a 50% fit error of ±0.012°C. For the salinity, the offset changed from −0.013 to 0.001 psu, with a 50% fit error of ±0.014 psu. The bow temperature and salinity are corrected using the fitted second-order polynomials. Combining the bow and thermosalinograph signals results in a near-surface dataset with both fine temporal/spatial resolution and high absolute accuracy.

d. *Velocity and acceleration*

The velocity measurements using the bow system are affected by vibration noise from the ship's body and bow platform, depending on the ship's speed and sea surface conditions. The vibrations are dependent on the ship's heading with respect to the surface wave field. The lowest vibrations are in the longitudinal direction, coincident with the axis line of the ship. The highest vibrations are in the transverse direction, perpendicular to the ship axis line. The nature of the vibration noise is principally different from that of measurements by towed vehicles. In the case of a towed device, the mechanical disturbance of the vehicle motion is primarily

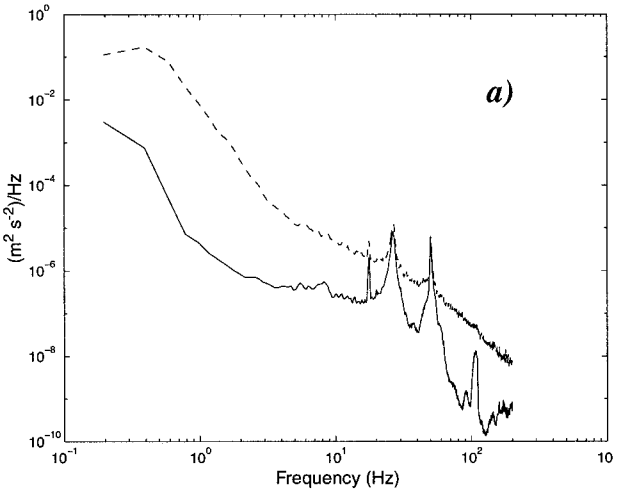

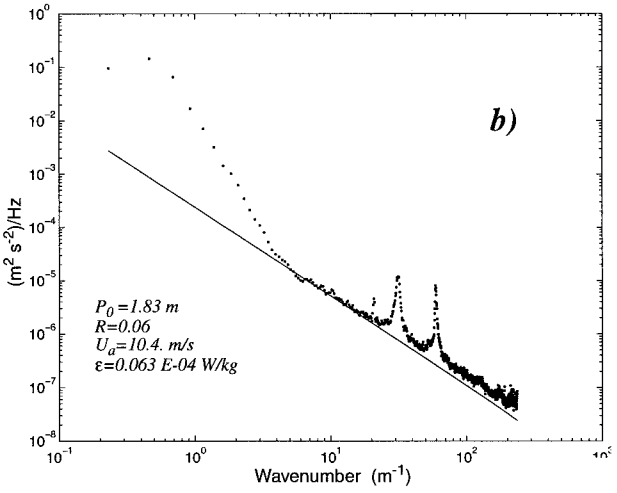

FIG. 11. (a) Spectrum of longitudinal (V_x) fluctuation velocity (dashes) in comparison to spectrum of integrated longitudinal (g_x) acceleration (solid line). (b) Wavenumber V_x spectrum (points) and theoretical spectrum of turbulence in inertial subrange. Ship speed is 10.3 kt.

due to the interaction of the vehicle with the tether line. This disturbance has a form of sudden, purely correlated pulses and has a wide frequency spectrum that practically cannot be removed from the signal. Moreover, such disturbances have a spectral form that is close to the spectrum of turbulence in the inertial subrange. Mechanical disturbance of the bow-mounted probes occurs mainly at certain relatively narrow resonant frequencies of the ship's body and bow platform. Such noise can be more easily detected and therefore effectively removed from the contaminated signal, provided the acceleration is measured. For this purpose, two acceleration sensors, ICSensors model 3145, were installed into

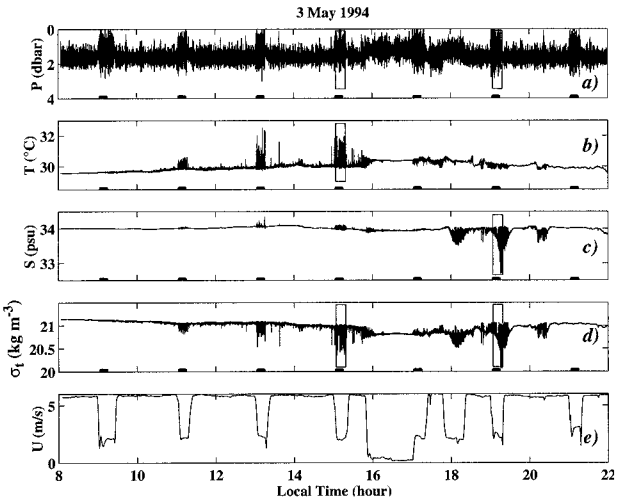

FIG. 12. Example of record made by bow sensors in the western Pacific warm pool (along 147°W) for a strong diurnal warming event. (a) Pressure, (b) temperature, (c) salinity, (d) density, and (e) ship speed. Segments marked by the boxes are used to plot the contour plots in Fig. 14 and 15. LST is for 147°W longitude.

the electromagnetic velocity probe during the EM and EQ-3 cruises.

Figure 11a shows examples of longitudinal velocity V_x and integrated acceleration g_x spectra for a 10.3-kt ship speed and 10.4 m s^{-1} wind speed. There are four vibration peaks between 16 and 110 Hz. Note the excellent agreement between the two sensors for the peak at 50 Hz, indicating the accuracy of the velocity sensor calibration. Three of the vibration modes are strong enough to contaminate the velocity spectrum noticeably. However, these peaks are relatively narrow. The technique of Stewart and Grant (1962)[1] can be used to estimate the dissipation rate of the turbulent kinetic energy from 10-min segments of the longitudinal V_x signal (Fig. 11b). This method yields $\varepsilon = 6.3 \times 10^{-6}$ W kg^{-1} for the spectrum shown in Fig. 11b.

5. Examples of at-sea data obtained during TOGA COARE

Figure 12 shows an example of the strong diurnal warming event in the near-surface layer of the ocean. High-frequency fluctuations of temperature T, salinity S, and σ_t are primarily a result of the depth variation of the probes. Until approximately 1600 local solar time (LST), the diurnal warming was mainly localized in the upper 1 m of the ocean (as a result of the prevailing calm weather conditions). The amplitude of the temperature high-frequency variability, therefore, strongly depended on the pitching depth range of the sensors.

[1] The universal spectrum of turbulence is fit to the data in the inertial-viscous subrange.

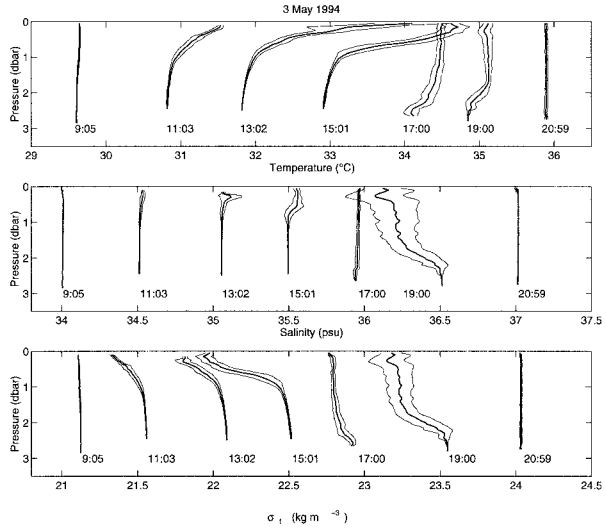

FIG. 13. Vertical profiles of temperature, salinity, and density obtained by averaging 10-min intervals of the bow sensors' data within 0.1-db pressure ranges. Each successive profile is shifted by 1°C in temperature, by 0.5 psu in salinity, and by 1.0 kg m^{-3} in σ_t. The time below each profile corresponds to the middle of the 10-min segment. Thin lines represent ± 1 std dev.

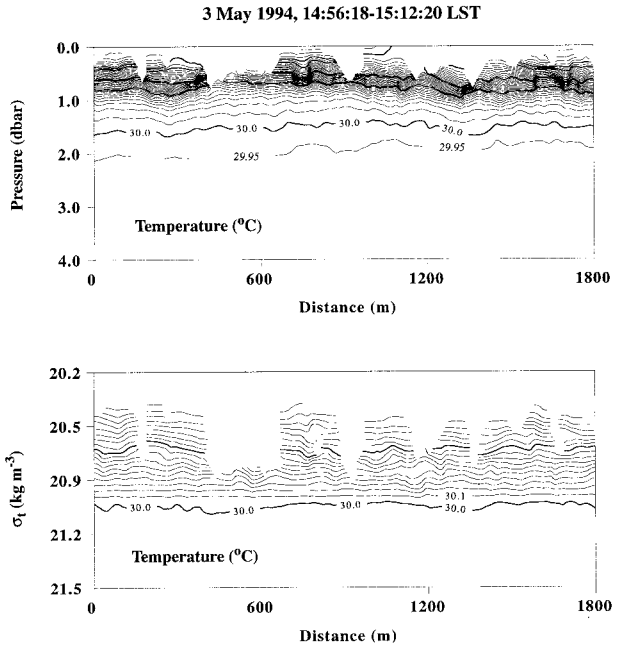

FIG. 14. Contour plots of T vs P and of T vs σ_t calculated during strong diurnal warming of the upper 1-m layer of the ocean (wind speed 2.2–2.4 m s^{-1}, ship speed 2.0 m s^{-1}).

To increase the pitching depth range of the bow sensors the research vessel collected approximately 15-min sample sections every 2 h during 3 May 1994 with decreased ship's speed ($\sim$2 m s^{-1}) and with the ship's heading into the surface waves.

The vertical profiles calculated from 10-min segments of the record during the sample sections illustrate the diurnal warming of the ocean under low wind speed conditions (Fig. 13). At 0905 LST, the profiles of T, S, and σ_t showed a well-mixed upper layer (within the 3-m depth variation range of the bow sensors). The temperature profile at 1103 LST indicated that the diurnal warming of the upper ocean layer had started. Because of low wind speed conditions, the diurnal thermocline was within the upper 1 m of the ocean. At 1302 LST, the diurnal thermocline was still in the upper 1 m because of calm conditions. The temperature difference across the diurnal thermocline sometimes achieved approximately 3°C. There was also approximately 0.1 psu salinity difference across the diurnal thermocline as a result of evaporation from the ocean surface and accumulation of the excess salinity within the diurnal mixed layer.

To study spatial structures, Soloviev and Lukas (1996) suggested calculation of the contour plots of temperature T, salinity S, and density σ_t using the variation of the probe's depth due to the vessel's pitching. The contour plot of the temperature field near 1500 LST is shown in Fig. 14. The corresponding section of the P, T, and σ_t records is denoted by rectangles in Fig. 12.

The vertical profiles of T, S, and σ_t at 1900 LST (Fig. 13) reveal the intersection of a surface freshwater lens. This time interval is shown in more detail in Fig. 15. The corresponding section of the record is denoted in Fig. 12 by rectangles. The salinity contour plot shows a leeward edge of the freshwater lens formed by a previous rain. There is a strong near-surface front in the

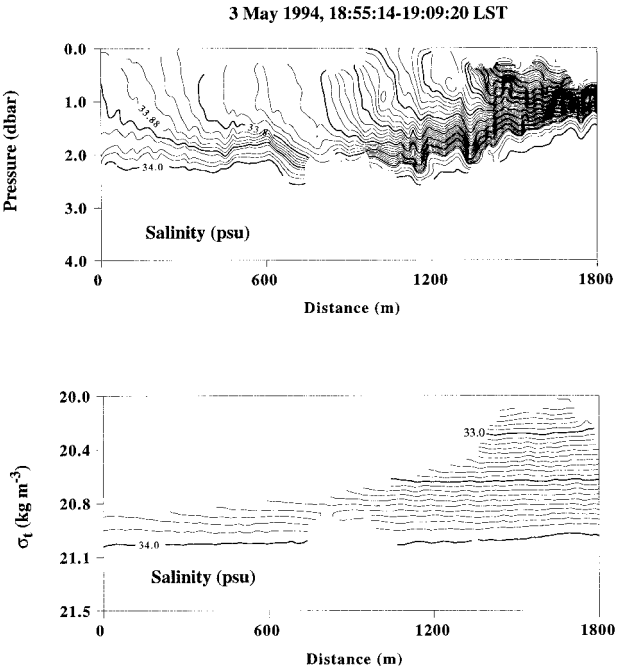

FIG. 15. Contour plots of S vs P and of S vs σ_t calculated during intersection of a surface freshwater lens (wind speed 2.7–4.6 m s^{-1}, ship speed 2.4 m s^{-1}).

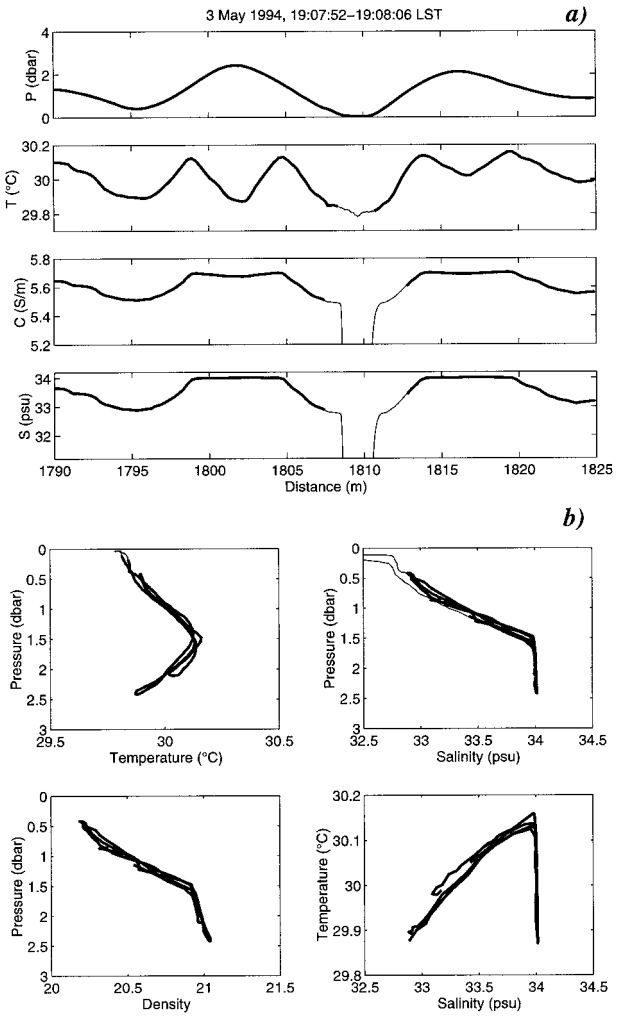

FIG. 16. (a) A segment of the *P*, *T*, and *S* record on 3 May 1994 at an intersection of the air–sea interface; (b) *T* and *S* as function of *P* and *T*–*S* diagram calculated from the segment shown in (a). Thin lines represent the raw signals, while the bold lines are the signals after processing.

upper 2 m of the ocean associated with spreading of this freshwater lens. The contour plot of salinity in density coordinate, however, shows no features.

An intersection of the air–sea interface by bow sensors during measurements on 3 May 1994 (see Fig. 12) is shown in Fig. 16a. Figure 16a includes the conductivity *C* record as well. The conductivity signal abruptly drops at approaching the sea surface. This happens at about 0.1-m depth, which is approximately equal to the spatial resolution of the conductivity cell (Table 2). Disturbed segments of *T*, *C*, and *S* (thin line) are automatically removed by the processing algorithm (section 4b). In Fig. 16b, *T*, *S*, and σ_t, plotted as function of the pressure are shown. These data (Fig. 16) are obtained within a strong freshwater lens (Fig. 15). A shallow freshwater layer and a temperature inversion are clearly seen in the upper approximately 1.5-m layer of the ocean (Fig. 16b). However, the density stratification is stable.

There are some differences between the successive salinity profiles measured at the intersection of the air–sea interface in the reciprocal directions (Fig. 16b). The differences between the successive temperature profiles are smaller.

6. Summary

A rugged bow-mounted system that provides measurements of temperature, salinity, and microstructure statistics in the near-surface regime was developed for COARE. The sensor characteristics, calibrations, response functions, and noise levels have been documented in this paper as well as the data processing algorithms. The sensors have been demonstrated to have excellent calibration stability. The calibration stability of the temperature and conductivity sensors coupled with algorithms that generate clean well-matched signals yield salinity data absent of salinity spikes over scales of 1.25 m. Vibration contamination, a key issue for velocity measurements, has been shown to occur in narrow-frequency bands that do not preclude accurate estimates of the kinetic energy dissipation rate.

The large vessel speed, 5–10 kt, provides scale separation between the orbital velocities of the surface waves and the turbulent velocity field; it also allows the use of Taylor's hypothesis to transform from the time domain to the spatial domain for estimation of turbulence statistics. The high-resolution pressure sensor, corrected each time the sensors surface, maintains a coordinate system fixed to the surface. The difficulties posed by the surface wave field have been largely eliminated.

Samples of the unique observations generated by this system are presented. Spatial structure of the near-surface layer can be studied as well as sample sets of turbulence statistics fixed in a reference frame anchored to the ocean surface. Further analysis, including estimates of turbulence statistics, of the dataset obtained during the COARE experiments should yield key insights into near-surface physics.

Acknowledgments. This work has been supported by NSF Grant OCE-9216891, ONR Grants N00014-961-0832 and N00014-96-1-0836, and by the P. P. Shirshov Institute of Oceanology Russian Academy of Sciences. Michael Gregg (University of Washington) suggested the inclusion of this work to the TOGA COARE IOP planners and provided the opportunity to collect measurements during the R/V *Moana Wave* COARE IOP-3 leg. Vadim Pelevin (P. P. Shirshov Institute of Oceanology) provided for the testing of the equipment during the Atlantic cruise of R/V *Academic Mstislav Keldysh* from June to August 1992. We thank Peter Hacker for useful discussions of the work. The ORSTOM/Noumea group SURTROPAC rendered substantial assistance in

the preparation of the apparatus. The assistance of the crew of R/V *Moana Wave* was crucial for success of the project. Calibrations of the temperature and conductivity sensors and the flow channel measurements were performed by William Drummond and Joseph Hopkins, respectively (The Johns Hopkins University Applied Physics Laboratory).

REFERENCES

Azizjan, G. V., Y. A. Volkov, and A. V. Soloviev, 1984: Experimental investigation of vertical thermal structure of thin boundary layers of the sea and atmosphere. *Izv. Atmos. Oceanic Phys.,* **20,** 511–519.

Bruce, J. G., and E. Firing, 1974: Temperature measurements in the upper 10 m with modified expendable bathythermograph probes. *J. Geophys. Res.,* **79,** 4110–4111.

Csanady, G. T., 1984: The free surface turbulent shear layer. *J. Phys. Oceanogr.,* **14,** 402–411.

Dillon, T. M., J. G. Richman, G. G. Hansen, and M. D. Pearson, 1981: Near-surface turbulence measurements in a lake. *Nature,* **290,** 390–392.

Farmer, D. M., and J. R. Gemmrich, 1996: Measurements of temperature fluctuations in breaking surface waves. *J. Phys. Oceanogr.,* **26,** 816–825.

Fedorov, K. N., and A. I. Ginzburg, 1992: *The Near-Surface Layer of the Ocean.* Koninklije Wohrmann BV, 259 pp.

Fozdar, F. M., G. J. Parker, and J. Imberger, 1985: Matching temperature and conductivity sensor response characteristics. *J. Phys. Oceanogr.,* **15,** 1557–1569.

Imberger, J., 1985: The diurnal mixed layer. *Limnol. Oceanogr.,* **30,** 737–770.

Jones, I. S. F., and B. C. Kenney, 1977: The scaling of velocity fluctuations in the surface mixed layer. *J. Geophys. Res.,* **82,** 1392–1396.

Kudryavtsev, V. N., and A. V. Soloviev, 1990: Slippery near-surface layer of the ocean arising due to daytime solar heating. *J. Phys. Oceanogr.,* **20,** 617–628.

Lukas, R., and E. Lindstrom, 1991: The mixed layer of the western equatorial Pacific Ocean. *J. Geophys. Res.,* **96** (Suppl.), 3343–3358.

Mammen, T. C., and N. von Bosse, 1990: STEP-A temperature profiler for measuring the oceanic thermal boundary layer at the ocean–air interface. *J. Atmos. Oceanic Technol.,* **7,** 312–322.

Osborn, T., D. M. Farmer, S. Vagle, S. A. Thorpe, and M. Cure, 1992: Measurements of bubble plumes and turbulence from a submarine. *Atmos.-Ocean,* **30** (3), 419–440.

Price, J. F., R. A. Weller, and R. Pinkel, 1986: Diurnal cycle: Observations and models of the upper ocean response to diurnal heating, cooling and wind mixing. *J. Geophys. Res.,* **91,** 8411–8427.

Shinoda, T., S. DeCarlo, S. Kennan, R. Lukas, F. Santiago-Mandujano, and J. Snyder, 1995: Shipboard measurements during COARE enhanced monitoring cruises. SOEST Tech. Rep. 95-07, School of Ocean and Earth Science and Technology, University of Hawaii, Honolulu, HI, 205 pp. [Available from Dept. of Oceanography, University of Hawaii at Manoa, 1000 Pope Road, Honolulu, HI 96822.]

Soloviev, A. V., 1990: Coherent structures at the ocean surface in convectively unstable conditions. *Nature,* **346,** 157–160.

——, and N. V. Vershinsky, 1982: The vertical structure of the thin surface layer of the ocean under conditions of low wind speed. *Deep-Sea Res.,* **29,** 1437–1449.

——, and R. Lukas, 1996: Observation of spatial variability of diurnal thermocline and rain-formed halocline in the western Pacific warm pool. *J. Phys. Oceanogr.,* **26,** 2529–2538.

——, N. V. Vershinsky, and V. A. Bezverkhnii, 1988: Small-scale measurements in near-surface layer of the ocean. *Deep-Sea Res.,* **35,** 1859–1874.

——, R. Lukas, S. DeCarlo, J. Snyder, A. Arjannikov, M. Baker, and D. Khlebnikov, 1995: Small-scale measurements near the ocean–air interface during TOGA COARE. Data Rep. SOEST 95-05, University of Hawaii, Honolulu, HI, 257 pp. [Available from Dept. of Oceanography, University of Hawaii at Manoa, 1000 Pope Road, Honolulu, HI 96822.]

Stewart, R. W., and H. L. Grant, 1962: Determination of the rate of dissipation of turbulent energy near the sea surface in the presence of waves. *J. Geophys. Res.,* **67,** 3177–3180.

Thorpe, S. A., 1985: Small-scale processes in the upper ocean boundary layer. *Nature,* **318,** 519–522.

Vershinsky, N. V., and A. V. Soloviev, 1977: A sounder for studies of the ocean surface layer. *Okeanologija,* **17,** 358–363.

Volkov, Ju. A., A. V. Soloviev, V. V. Turenko, V. A. Bezverkhnii, N. V. Vershinsky, and F. M. A. Ermolaev, 1989: Investigation of hydrophysical structure of the thin surface layer of the ocean from a moving vessel. *Izv. Atmos. Oceanic Phys.,* **25,** 695–701.

Webster, P. J., and R. Lukas, 1992: TOGA COARE: The Coupled Ocean–Atmosphere Response Experiment. *Bull. Amer. Meteor. Soc.,* **73,** 1377–1416.